Available online at www.sciencedirect.com

ScienceDirect

International Journal of Plasticity 24 (2008) 1440–1456

INTERNATIONAL JOURNAL OF Plasticity

www.elsevier.com/locate/ijplas

Plastic behavior of a nickel-based alloy under monotonic-tension and low-cycle-fatigue loading

E-Wen Huang [a], Rozaliya I. Barabash [b,c,*], Yandong Wang [a,d], Bjørn Clausen [e], Li Li [a], Peter K. Liaw [a], Gene E. Ice [b], Yang Ren [f], Hahn Choo [a], Lee M. Pike [g], Dwaine L. Klarstrom [g]

[a] *Department of Materials Science and Engineering, University of Tennessee, Knoxville, TN 37996, USA*
[b] *Materials Science and Technology Division, Oak Ridge National Laboratory, Oak Ridge, TN 37831, USA*
[c] *Center for Materials Processing, University of Tennessee, Knoxville, TN 37996, USA*
[d] *Key Laboratory for Anisotropy and Texture of Materials, Ministry of Education, Northeastern University, Shenyang 110004, PR China*
[e] *Los Alamos Neutron Science Center, Los Alamos National Laboratory, Los Alamos, NM 87545, USA*
[f] *X-ray Science Division, Argonne National Laboratory, Argonne, IL 60439, USA*
[g] *Department of Technology Engineering, Haynes International Inc., Kokomo, IN 46904, USA*

Received 25 July 2007; received in final revised form 1 October 2007
Available online 16 October 2007

Abstract

The plastic behavior of an annealed HASTELLOY® C-22HS™ alloy, a face-centered cubic (FCC), nickel-based superalloy, was examined by in-situ neutron-diffraction measurements at room temperature. Both monotonic-tension and low-cycle-fatigue experiments were conducted. Monotonic-tension straining and cyclic-loading deformation were studied as a function of stress. The plastic behavior during deformation is discussed in light of the relationship between the stress and dislocation-density evolution. The calculated dislocation-density evolution within the alloy reflects the strain hardening and cyclic hardening/softening. Experimentally determined lattice strains are compared to verify the hardening mechanism at selected stress levels for tension and cyclic loadings. Combined with calculations of the dislocation densities, the neutron-diffraction experiments provide direct information about the strain and cyclic hardening of the alloy.
Published by Elsevier Ltd.

---

[*] Corresponding author. Address: Materials Science and Technology Division, Oak Ridge National Laboratory, Oak Ridge, TN 37831, USA. Tel.: +1 865 241 7230.
E-mail address: barabashr@ornl.gov (R.I. Barabash).

0749-6419/$ - see front matter Published by Elsevier Ltd.
doi:10.1016/j.ijplas.2007.10.001

Keywords: Plasticity; Dislocations; In-situ neutron-diffraction; Fatigue

1. Introduction

The design of advanced metal alloys requires detailed information about the mechanical behavior and property evolution in service beyond elasticity, which is roughly independent of defects. Plasticity and the underlying deformation mechanisms evolve during service. In metals, dislocations are responsible for most of the plastic deformation. During deformation, these dislocations multiply and self-organize into mesoscale structures that strongly influence future deformation. However, Guinier and Julien (1989) has pointed out the challenge of studying dislocations, especially for fatigue, in light of the sample preparation required for electron microscopy. In the present work, monotonic-tension and cyclic-loading during in-situ neutron experiments have been used to compare and study the fatigue behavior of a superalloy. Understanding the plastic behavior of this newly-designed nickel-based superalloy is important for applications in extreme environments. In-situ neutron-diffraction experiments provide non-destructive, volume-averaged bulk characterization of the atomistic mechanisms with qualitative trends for studying the plastic deformation of the alloy. The focus of current research is associated with dislocation evolution during plastic deformation.

Transmission-electron-microscopy (TEM) (Hirsch and Whelan, 1960; Howie and Whelan, 1962) is well established for the study of local structures and the internal stresses contributed by dislocations. However, with TEM, only a small amount of material is observed with each thin specimen and the statistics and the response of the experimental are limited by the demanding sample preparation. X-ray experiments provide an alternative method for studying dislocation structures, which complement TEM experiments. X-ray diffraction experiments with advanced analyses have characterized different types of dislocations (Mughrabi, 1983; Ungar et al., 1999; Barabash et al., 2003). Anisotropic strain accommodations by different grains were considered by Stephens (1999). Recently, Jakobsen et al. (2006) and Levine et al. (2006) report the use of the synchrotron X-ray accompanying TEM results to study local dislocation behavior during plastic deformation. These studies illustrate the potential of diffraction techniques for the investigations of dislocation behavior in plastic deformation. The current study reports in-situ neutron-diffraction measurements that utilize the advantage of the diffraction experiments for examining dislocation statistics associated with plastic deformation. The advantages of the present neutron measurements are:

- The high penetration of neutrons characterizes bulk behavior with large gauge volumes, and, hence, good statistics (Wang et al., 2003). Although the divergence of the neutron beams is higher than that of high-energy synchrotron X-rays, the typically lower resolution of neutron measurements is sufficient for our research, which focuses on statistical averages.
- The Spectrometer for MAterials Research at Temperature and Stress (SMARTS) (Bourke et al., 2002) at the Los Alamos Neutron Science Center (LANSCE) can be used to conduct in-situ measurements to observe the behaviors of the deformation from a single specimen. The in-situ measurement eliminates confusion from ex-situ experiments that require several specimens and associated sample preparations.

The current study focuses on the plastic behavior of a nickel-based alloy under tension and cyclic loadings. To address this problem, the in-situ neutron measurements were designed with these components:

[1] Tension experiments were conducted to study strain hardening mechanisms and the associated dislocation-density evolution.
[2] Low-cycle-fatigue experiments were performed to study cyclic hardening and softening, and the dislocation-density evolution.
[3] Dislocation densities as a function of the true stress from strain hardening, cyclic hardening, and cyclic softening are compared with the lattice strain evolutions to examine the plastic behavior of the alloy.

2. Test materials and experiments

The HASTELLOY® C-22HS™ alloy is a nickel-based superalloy (Ni–21Cr–17Mo in the weight percentage). The alloy is intended to be used under corrosive environments and where high strength is demanded. The alloy is mill annealed at 1080 °C to minimize the formation of precipitates and to achieve a single-phase, face-centered cubic (FCC) alloy, as characterized by transmission-electron-microscopy (TEM) (Lu et al., 2007). The average grain size of this alloy is about 90 μm.

Two sets of the specimens, one for tension and the other for fatigue were cut from the same cylindrical alloy bar. The dimensions of the dog-bone shape specimens were selected according to the standard ASTM/E 606 as shown in Fig. 1a. In-situ neutron measurements were used to monitor the monotonic-tension and low-cycle-fatigue experiments. A gauge volume of about 120 mm^3 from the center of the specimen was used through both the measurements of monotonic-tension and low-cycle-fatigue experiments. The tests were carried out with the SMARTS beamline of LANSCE and the environment is at room temperature (Benson et al., 2006; Sun et al., 2007). The specimens were aligned 45° to the incident neutron beam with two detector banks fixed at $2\theta = \pm 90°$. Hence, one detector bank collected diffraction data along the loading direction ($Q_{\|}$), and the other collected the diffraction data in the transverse direction ($Q_{\perp}$) as shown in Fig. 1b. The Q directions are associated with two distinct sets of grains: $Q_{\|}$ measures lattice strain for $\{hkl\}$ planes parallel to the strain; and $Q_{\perp}$ measures lattice strain perpendicular to tension load. Practically grains with surface normals in the interval of ±4° relative to the exact Bragg condition give input to the diffraction. Since the beam paths are slightly different for loading to transverse directions (Fig. 1b and c), we use reference points accordingly for peak-profile analyses.

For the tension experiment, the sample was loaded in strain control using a strain rate of 0.001 s^{-1} with intermittent holds at constant strain levels to allow for neutron-diffraction measurements. The specimen was elongated to a strain of about 45% and then failure. The closest measurement before necking is at about 32% strain. The stress–strain curve of the in-situ tension experiments is presented in Fig. 2. The onset of the plastic deformation is marked in the green region and is enlarged as the inset plot. The 0.2% yield stress is around 370 MPa, which will be a reference for the evolution of dislocations. Load drops are seen in the plastic region during the constant strain holds due to room temperature relaxation. The count time for a single neutron-diffraction measurement is about 10 min.

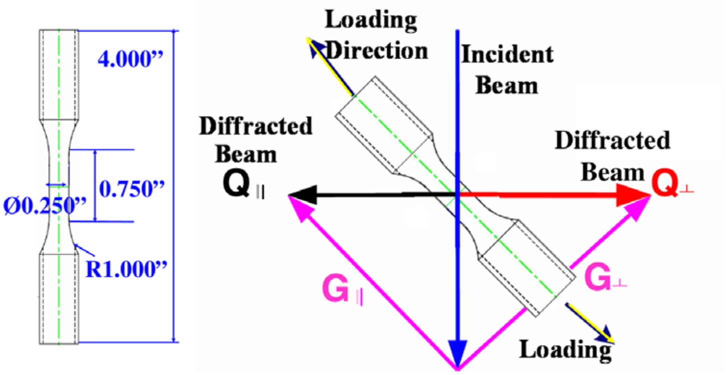

(a) Specimen geometry (b) Neutron beam path

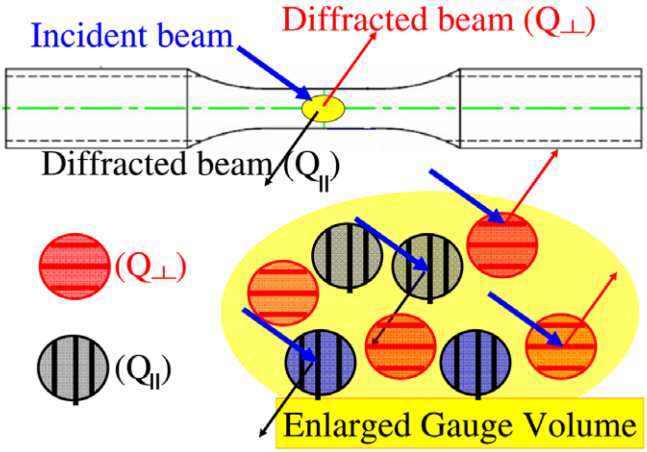

(c) Schematic grain-oriented-dependent diffraction

Fig. 1. (a) The geometry of the specimen. (b) A schematic view of the neutron beam path for measurement. (c) The schematic plot shows that only the grains satisfying Bragg's condition diffract the incident neutrons to the detector banks. The grains with $\{hkl\}$ planes along loading direction ($Q_{\|}$) are shown in gray. The grains with $\{hkl\}$ planes in the transverse direction ($Q_{\perp}$) are shown in red.

The low-cycle-fatigue experiments were conducted with a minimum strain ($\varepsilon_{\mathrm{min.}}$) and maximum strain ($\varepsilon_{\mathrm{max.}}$) of −1% and +1%, respectively ($R = -1$). The frequency of the loading cycle was 0.5 Hz. The neutron-diffraction data were collected at several selected cycles during the fatigue experiments within 1500 cycles. The cyclic-loading sequence in Fig. 3a shows the deformation status during the measurements. The specimen was loaded to a maximum engineering strain of 1% at Measurement 1. At Measurement 2, the sample was unloaded to 0 MPa. At Measurement 3, the sample was compressed to a macro-strain of 0%. At Measurement 4, the sample was compressed to an engineering strain of −1%. At Measurement 5, the sample was unloaded from the compression to 0 MPa. At Measurement 6, the sample was loaded to 0% engineering strain. The 7th measurement (Measurement 7) is made at the 1% engineering strain again to compare with Measurement 1 for cyclic effects within one fatigue cycle. Neutron measurements were performed at these seven measurement points as a function of fatigue cycles. The macroscopic stresses at

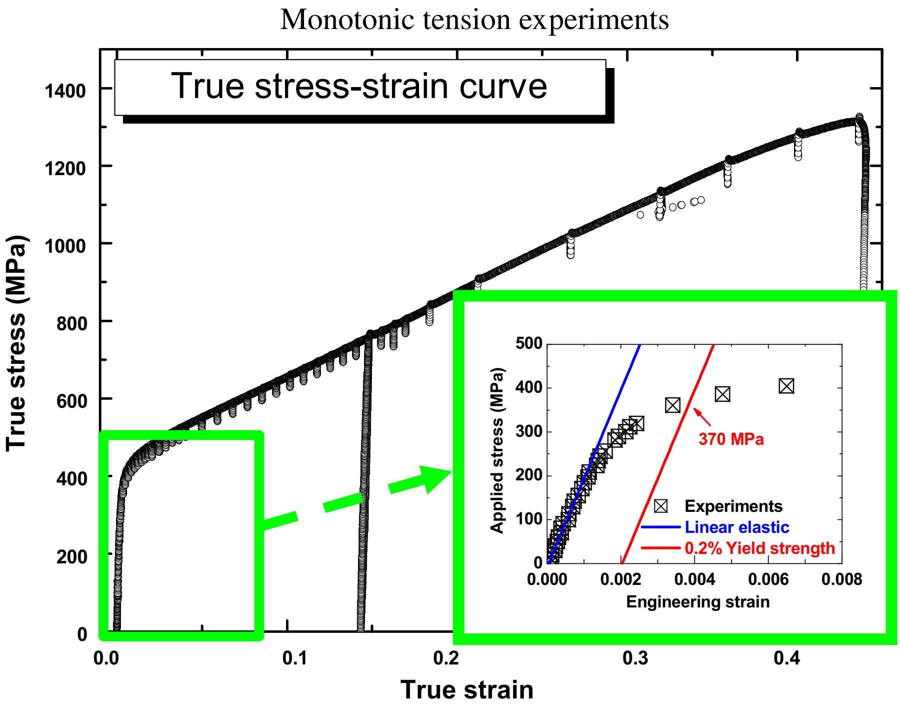

Fig. 2. True stress–true strain curve of the alloy for the monotonic experiment. The intersection is the enlargement of the early straining curve to show the onset of the plastic deformation.

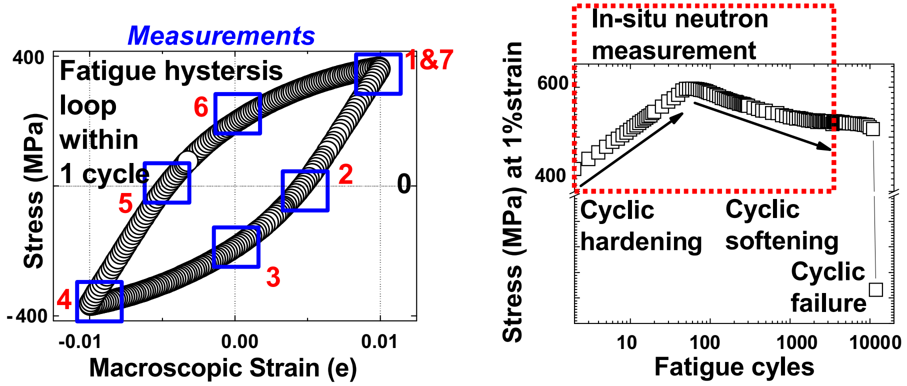

(a) Seven Measurements (b) Cyclic loadings

Fig. 3. (a) Seven measurements of the low-cycle-fatigue experiments within one fatigue cycle. (b) Stress at 1% strain (Measurement 1) is plotted as a function of fatigue cycles. Several in-situ neutron experiments were conducted within 1500 fatigue cycles. In the beginning, the stress increase as fatigue cycle increases until 600 MPa at 100th cycle, and then decreases.

Measurement 1 as a function of the fatigue cycles are presented in Fig. 3b (Huang et al., 2007). The experiments conducted at Measurement 1 of the fatigue cycles mentioned above are compared with the results from the monotonic-tension experiments.

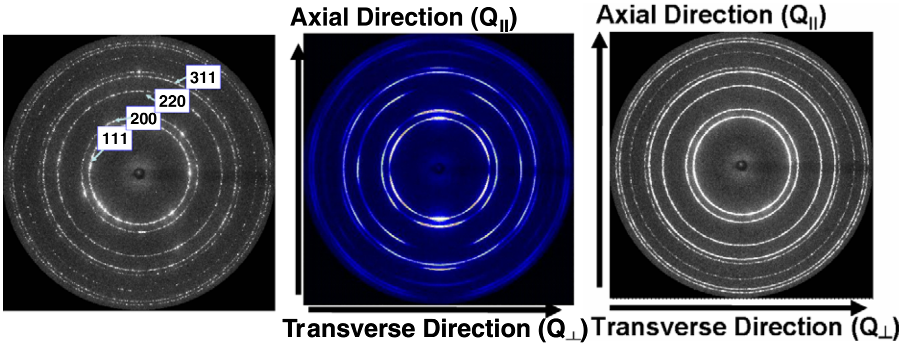
311
220
200
111
Axial Direction ($Q_{||}$)
Transverse Direction ($Q_{\perp}$)
Axial Direction ($Q_{||}$)
Transverse Direction ($Q_{\perp}$)

(a) Undeformed (b) Tension-deformed (c) Cyclic-deformed

Fig. 4. The high-energy synchrotron-diffraction patterns collected from the (a) undeformed alloy, (b) tensile-deformed specimen, and (c) cyclic-deformed specimen. As the arrows depicted, the intensity of different diffraction rings can be compared with respect to the axial and transverse directions.

Synchrotron X-ray diffraction (XRD) experiments were conducted to complement the neutron measurements. The high-energy (115 keV) X-ray diffraction experiments were performed at the 11-ID-C beamline of the Advanced Photon Source, Argonne National Laboratory. The size of the X-ray beam was controlled to 1.0 × 1.0 mm^2 to collect diffraction data with good statistics. Undeformed, tension-failed, and cyclic-failed specimens were prepared for the synchrotron experiments. Slices were cut from the center of the mechanically-tested specimens, which were deformed under the monotonic tension and low-cycle-fatigue tests. The cut materials were then polished to remove the oxides and other additives to eliminate contaminations associated with the sample preparation. The diffraction patterns were recorded using a two-dimension (2D) image plate detector (Mar345). The symmetry of the diffraction rings, as shown in Fig. 4, indicates that the textures of the undeformed, tensioned, and cyclically-deformed specimens were symmetrical, and, hence, the depiction of the two detector banks data from the SMARTS measurements is representative for describing the evolution of the elastic/plastic response of the material during the deformation. The most distinguished difference from monotonic-tension to cyclic deformation is that there is texture developed after the monotonic-tension (Wenk and Grigull, 2003) but texture development is not seen during cyclic deformation [compare solid and spotty characters of the diffraction rings in Fig. 4b and c]. Turkmen's modeling work (Turkmen et al., 2002) also finds little texture evolution under cyclic loading.

3. Neutron-data analyses

The current in-situ neutron-diffraction profiles are refined by the General Structure Analysis System (GSAS) (Von Dreele et al., 1982; Von Dreele, 2004) which is based on full-pattern Rietveld analysis method (Rietveld, 1967). The changes in the peak positions and the peak widths are determined from the diffraction patterns and presented as the lattice strain and full-width-half-maximum (FWHM), respectively.

For the profile analyses, there are several sources of diffraction peak broadening, such as instrument broadening, the size of the coherently-scattering domains, dislocations (defects) (Ungar et al., 1999; Balzar et al., 2004; Barabash, 2001; Ice and Barabash, 2007), and the anisotropic strain distribution (Stephens, 1999). For the current study, since the same alloys are tested with the same instruments, the instrumental broadening was measured from the diffraction profile of a reference sample (before the deformation) and was used to remove instrumental broadening from the total broadening.

As shown in Fig. 1b, the diffracted beam path is shorter in the transverse-direction ($Q_{\perp}$) than that in the loading direction ($Q_{\|}$). Since the difference of the beam path might alter the diffracted peak-profile, the peak-profile analyses used different references with respect to different directions according to account for this geometry anisotropy. However, since correlation between the neutron-beam path to the peak-width is not necessary linear, there is no universal equation to normalize the geometrical anisotropy.

We use two distinct approaches to describe the appearance of line broadening: phenomenological and atomistic lattice level. In the phenomenological approach, the shift of the peak depends on the macroscopic stress, and the broadening of the peak is related to micro-strains/stresses that change from grain to grain. Measurements of the peak shift during the deformation allow us to follow the evolutions of such phenomenological parameters as macro-stresses and -strains. There are several types of strains that could contribute to the peak-width broadening, such as intergranular and intragranular strains. Different types of strains arise from the various microstructures, such as different types and densities of dislocations. The lattice or atomistic approach can be used to understand the dependence of the broadening on the particular dislocation/defect distributions within the grain. Peak-profile analyses provide statistical information about the dislocation density evolution under deformation.

To decompose the broadened asymmetric peaks into two broadened symmetric sub-peaks, the pseudo-Voigt function is applied to carry out single-peak fitting to distinguish the different diffraction patterns by GSAS (Balzar et al., 2004). The Lorentzian and Gaussian peak-broadening components were de-convoluted by a pseudo-Voigt function in GSAS (Von Dreele, 2004). The FWHM of Gaussian ($\mathrm{FWHM_G}$) and Lorentzian ($\mathrm{FWHM_L}$) components were characterized as a function of the stress, respectively because the integrated intensities of these two sub-peaks (Gaussian and Lorentzian) are related by random dislocations and dislocation walls, respectively. The procedure is similar to size/strain separation (Balzar et al., 2004). As a result, the smaller sub-peak is diffracted by the cell walls, and the larger one comes from the cell interiors as homogenously distributed dislocations (Levine et al., 2006). $\mathrm{FWHM_G}$ represents the input which can be generated by the uniform randomly distributed dislocations, while $\mathrm{FWHM_L}$ indicates the input from the non-uniform patterned dislocations substructures, such as the dislocation walls (Mughrabi, 1983; Barabash, 2001). The spacing between dislocation walls (D) is calculated according to the following equation (Barabash, 2001; Ice and Barabash, 2007):

$$D \sim \frac{\pi\zeta}{\mathrm{FWHM_L}} \tag{1}$$

Here ζ is the contrast factor, used to calculate the Lorentzian part, from the whole powder-pattern fitting of peak-profile. As a first approximation, the dislocation density is calculated, assuming equal dislocation activity for all primary slip systems. The density (n) of the randomly distributed dislocations is calculated according to the following equation (Barabash, 2001; Ice and Barabash, 2007):

$$n \sim \left(\frac{\mathrm{FWHM_G} \times d_{hkl}}{C \times |b|} \right)^2 \tag{2}$$

Here the Burgers vector (b), the contrast factor (C) for the Gaussian component, the d_{hkl}-spacing for each $\{h\,k\,l\}$ plane, and the $\mathrm{FWHM_G}$ of all $\{h\,k\,l\}$ planes are considered.

The lattice strains, ε_{hkl}, are calculated by the changes in the d-spacing, d_{hkl}, at different applied loads during the monotonic-tension experiment or at different number of fatigue cycles for low-cycle-fatigue experiments with respect to that of the reference d-spacing, d^0_{hkl}, as shown in the following equation (Daymond et al., 1997):

$$\varepsilon_{hkl} = \frac{d_{hkl} - d^0_{hkl}}{d^0_{hkl}} \tag{3}$$

The reference lattice spacing, d^0_{hkl}, was determined from the measured lattice spacing before deformation.

4. Results

Plots of the FWHM versus $2\pi/d$ as a function of stress for tension experiments and low-cycle-fatigue experiments are shown in Fig. 5. Here d is the d-spacing. In the monotonic experiments, correlations between the FWHM and $2\pi/d$ deviates from linearity as the strain increased, while the applied stress increased. For the low-cycle-fatigue experiments, the correlations changed as a function of fatigue cycles, where the engineering strain was controlled at 1% at Measurement 1, the applied stress varies as a function of fatigue cycles. FWHM for both types of loading are markedly anisotropic depending on $\{h\,k\,l\}$ which is in agreement with the previous observations of Ungar et al. (1999) and Sun et al. (2007). This is an indication of the formation of the patterned cell wall dislocation substructure.

4.1. Dislocation density and dislocation-wall spacing evolutions

For the monotonic-tension experiment, the dislocation density as a function of the true stress is shown in Fig. 6a. The following three regions are distinct:

- Stage I (0–370 MPa): the region of the elastic straining is a stage where stresses increased as the strain increased, as shown in the stress–strain curve (Fig. 2), while the dislocation density practically does not change too much (Fig. 6a). The calculated dislocation-wall spacings are large (>1500 nm) and fluctuate in both $Q_\perp$ and $Q_\parallel$ directions in Fig. 6b. However, the accuracy of the neutron-diffraction measurements is inadequate for characterizing cell size larger than 1500 nm, hence, larger symbol sizes are plotted for the calculated values at Stage I.
- Stage II (370–750 MPa): the dislocation-strengthening region where the dislocation density is proportional to the true stress. In this region, the stresses are high enough so that dislocations start to multiply and pile-up, and, hence, increase the back stress, which resists the motion of additional dislocations. The dislocation density starts to increase rapidly at about 370 MPa. At this stress value, the dislocation sources became activated meanwhile the dislocation-wall spacings decreased in $Q_\perp$ and $Q_\parallel$ directions simultaneously and reached 800 nm.

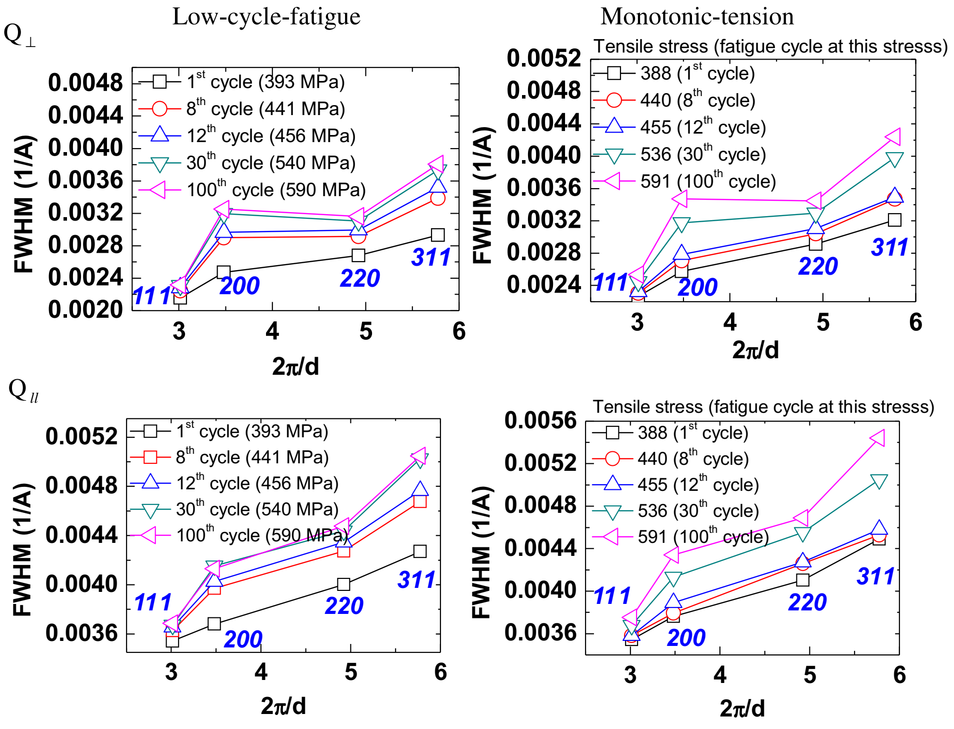

Fig. 5. FWHM versus $2\pi/d$ for low-cycle-fatigue and monotonic-tension experiments in $Q_\perp$ and $Q_\parallel$ directions.

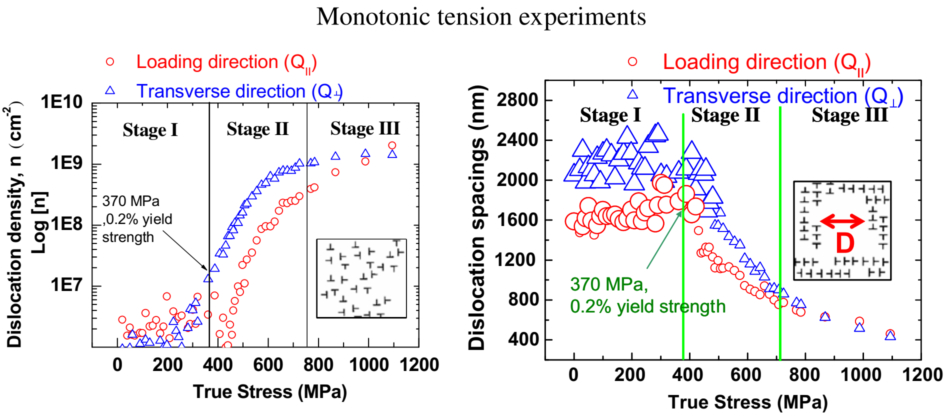

(a) Dislocation density (b) Dislocation walls spacing

Fig. 6. (a) The dislocation density versus true stress. The line between Stages I and II represents the macroscopic 0.2% yield strength. The inset shows a scheme of the randomly distributed dislocations at the bottom-right corner. (b) Dislocation-wall spacing within dislocation walls as a function of the true stress. The dislocation-wall spacing (D) is shown in the inset of the upper-right corner. The larger legends of (b) shows the higher uncertainty for the size greater than 1500 nm. For clarity, the data is plotted for along (‖) and (⊥) perpendicular to the loading direction.

- Stage III (above 750 MPa): the dislocation density gradually saturated with increasing stress in $Q_\perp$ direction but not too much in $Q_\parallel$ direction. The dislocation-wall spacing in $Q_\perp$ and $Q_\parallel$ directions decreased from 800 to 400 nm, where the sample is close to necking. At the point of *macro-yielding*, the dislocation-wall spacings possess the essential trend of the stress–strain curve, which does not change slope from 370 to 1200 MPa (Fig. 2). The value of the domain size is 400 nm (30% strain of the stress–strain curve), which is comparable to what is observed by Valiev et al. (2000). The reasonable mechanism is Mughrabi (1983) cell-wall structure, which views the evolution from homogeneous dislocation distribution to the heterogeneous dislocation cell wall structure consisting of the soft channels and the periodic array of the hard walls. The reason for this evolution trend is the compatibility to the changing shear strain fields, which is a continuum manifestation of the change of the heterogeneous channel-cell wall structure. It also suggests that the dislocation arrangements develop to lower-energy heterogeneous configurations compared to homogeneously distributed dislocations.

For low-cycle-fatigue experiments, at the 1% strain level, cyclic hardening started around 370 MPa until about 600 MPa, and is, then, followed by cyclic softening. Fig. 7a shows the dislocation density as a function of fatigue cycles. The dislocation density increased as the stress increased and, then, saturated and mildly decreased as a function of fatigue cycles. The dislocation density of low-cycle-fatigue experiments has approximately the same value as the monotonic experiments around the same true stress level as shown in Fig. 6a. The true stress region at 1% strain (Measurement 1) within 1500 fatigue cycles (Fig. 3b) corresponds to the interval of 400–600 MPa. For comparison between cyclic-loading and monotonic-tension, the same stress range is highlighted in the Stage II of the monotonic experiments. A comparison of the two experiments will be made within 400–600 MPa for lattice strain in the next section. The calculated dislocation-wall spacings evolved in a reverse relation to the dislocation density as shown in

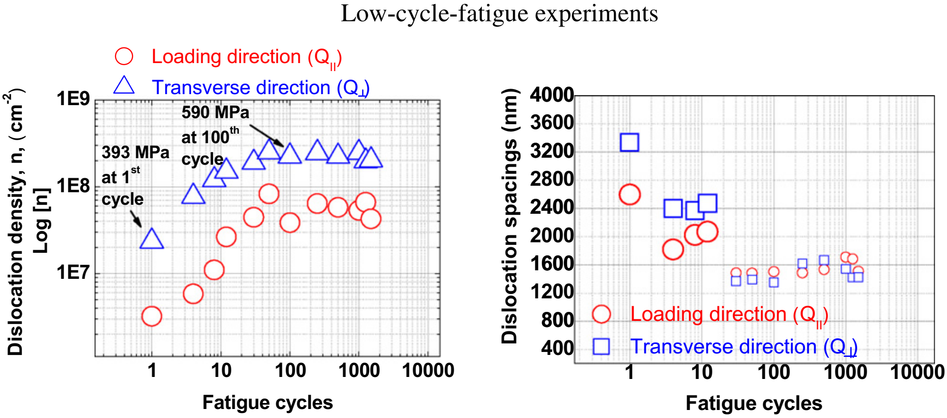
Low-cycle-fatigue experiments

(a) Dislocation density (b) Dislocation walls spacing

Fig. 7. (a) The dislocation density and (b) dislocation-wall spacings as a function of fatigue cycles at 1% strain. *Note:* The bigger legends of (b) in early fatigue cycles show the bigger fluctuations for the measured size greater than 1500 nm. For clarity, the data is plotted for along (‖) and (⊥) perpendicular to the loading direction. The true stress is 393 MPa at 1st and 590 MPa at 100th fatigue cycles.

Fig. 7b. Again, for dislocation-wall spacings exceeding 1500 nm, the larger legend-symbol size indicates larger error bars.

A clear anisotropic quantitative difference of dislocation density from the loading to the transverse directions under tension is due to the fact that intensity distributions for loading and transverse directions come from two orthogonal sets of grains as shown in Fig. 1c. Only grains which satisfy Bragg's condition will contribute to diffraction. For example, grains with {2 0 0} planes perpendicular to loading direction will give {2 0 0}-diffraction peaks into loading direction ($Q_{\|}$). Grains with the same planes {2 0 0} but oriented orthogonally to the loading direction diffract neutrons into the transverse-direction ($Q_{\perp}$) detectors. These two sets of grains are orthogonal to each other and have different Schmidt factors where Schmidt factor is distinct to different slip system, and, hence, resulted in different dislocation density in the grains with different orientations (Liu et al., 1998; Margulies et al., 2001; Hansen, 2001).

4.2. Lattice strain evolutions

Single-peak fitting was applied to study "lattice strain" evolution. The lattice strains of the monotonic-tension experiment, ε_{hkl}, are calculated from changes in the *d*-spacing, d_{hkl}, at different applied loads with respect to the reference *d*-spacing, d^0_{hkl} in Eq. (3). The reference lattice spacing, d^0_{hkl}, was determined from the measured lattice spacing before deformation (nominal tensile load of 0.099 MPa to ensure the sample did not sag in the horizontal loading geometry):

$$\varepsilon_{hkl} = \frac{d_{hkl} - d^0_{hkl}}{d^0_{hkl}} \tag{3}$$

The evolutions of the lattice strains of the monotonic-tension experiment showed that the response of the lattice strains in the elastic region of the applied load (region I in Fig. 6a) followed Hooke's relationship, and the stiffness of {1 1 1} plane is the largest, {2 0 0} is the least, and {2 2 0} and {3 1 1} are in between. Similar trends were observed during in-situ neutron-diffraction measurements on a face-centered cubic (FCC) stainless steel by Daymond et al. (1997). For the low-cycle-fatigue experiments, the lattice strains, ε_{hkl}, are calculated in the same fashion as the monotonic-tension experiment at different fatigue cycles with respect to that of the reference *d*-spacing, d^0_{hkl}. The reference lattice spacing, d^0_{hkl}, was determined from the measured lattice spacing before the cyclic-loading. A similar response was observed (Huang et al., 2007) from low-cycle-fatigue experiment although the whole measurements were conducted at a 1% engineering strain. Lattice strains increased as the cyclic hardening continued until an apex stress at 600 MPa where the stress began to decrease as softening starts to take place, and, hence, the lattice strains decreased.

To clarify the effects of the plastic deformation from two experiments, the elastic portion of the lattice strains were subtracted from the lattice strains as in Fig. 8a for low-cycle-fatigue tests and Fig. 8b for monotonic-tension experiments, respectively. The {1 1 1} and {2 0 0} of two different experiments have the comparable trends and levels while the {2 2 0} and {3 1 1} are not as alike. This difference may be caused by the texture formation during monotonic-tension experiments, which is in agreement with our XRD results (Fig. 4). More details of the strain-related texture formation have been reported (Miller et al.,

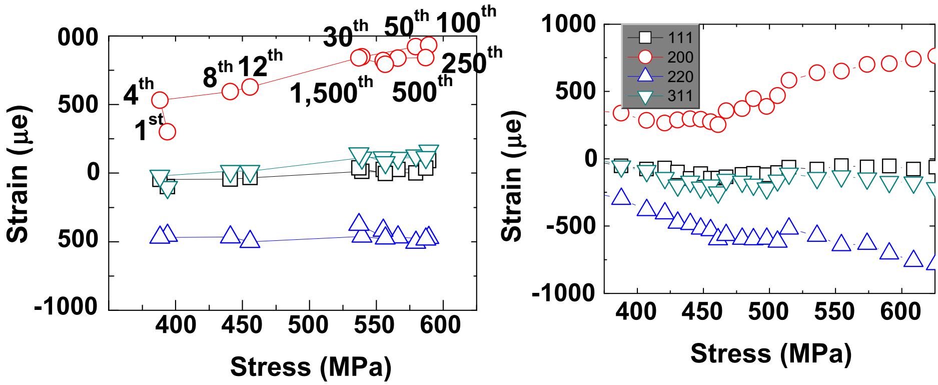

(a) Low-cycle-fatigue (b) Monotonic-tension

Fig. 8. Intergranular strains as a function of true stress in the same stress levels (the elastic portion of the lattice strains were subtracted from the measured lattice strains) of (a) low-cycle-fatigue experiments at Measurement 1 (fatigue cycles are marked along peak 200) and (b) monotonic-tension experiments.

2005; Bernier and Miller, 2006). From current study, the evolutions of lattice strain during both cyclic-loading (up to 100th cycle) and tension experiment (Stage II) reached similar values at the same true stress levels, which suggests further study. Since the true stress level of the Stage III of monotonic tension experiments was beyond that of the low-cycle-fatigue experiments, more research is needed to discover the different failure mechanisms.

5. Discussions

For monotonic experiments, the dislocation density is a good reference for the deformation process. The onset of Stage II is very close to the 0.2% yield strength, which supports the dislocation density calculation (Fig. 6a). The peak-broadening indicates intensive plastic deformation which resulted from an increase of the dislocation density. The inverse behavior between dislocation density (Fig. 6a) and dislocation-wall spacing (Fig. 6b) as a function of stress are similar to the observations of Hansen (2001 and 2005). When the dislocation density as a function of the stress starts to transit to Stage III, there is a slowdown in the rate of the dislocation density multiplication in both directions. Moreover, it saturates in $Q_\perp$ direction (Fig. 6a) around 700 MPa, which indicates that the multiplication of dislocation density decelerates. However, the dislocation-wall spacings decrease at the same rate in both Stages II and III, which indicates that the dislocations pile-up as stress increases and self-organize as a function of the stress. A similar statement has been proposed by Kuhlmann-Wilsdorf's TEM works (1962 and 1999), which suggests that the character of the dislocation distribution remains unchanged, and only the scale of the distribution changes. With further deformation, beyond Stage II, the number of free dislocations within the cells gradually keeps steady to the point where glide dislocations may move relatively unhindered from one cell wall to other cell walls (Kuhlmann-Wilsdorf, 1962, 1999).

For the low-cycle-fatigue experiments, since the cyclic hardening starts around 400 MPa and is about to end at the 100th fatigue cycle around 600 MPa, the peak widths broaden accordingly, and, then, the widths reduce, with the cyclic softening. The calculated dislocation density is shown in Fig. 7a. The dislocation density of the monotonic-tension experiments under same true stress region is shown in Fig. 6a for comparison.

It is interesting to compare the intergranular strains $\left(\varepsilon^{I}_{hkl}\right)$ of the two types of deformation. The lattice strains (ε_{hkl}) after subtracting the elastic part for both experiments are calculated, where the elastic strains are calculated based on the elastic modulii (E_{hkl}) and the true stress (σ). The evolutions of ε^{I}_{hkl} under monotonic-tension for all $\{hkl\}$ planes in $Q_{\perp}$ direction (Fig. 8a) are compared to those of the low-cycle-fatigue experiments at 1% strain as shown in Fig. 8b. These calculated lattice strains from Eq. (4) are intergranular strains $\left(\varepsilon^{I}_{hkl}\right)$ from the combined effects of the elastic anisotropy, thermal anisotropy, and plastic anisotropy (Brown et al., 2003). Here, the elastic response is subtracted from measured lattice strains:

$$\varepsilon^{\mathrm{I}}_{hkl} = \varepsilon_{hkl} - \frac{\sigma}{E_{hkl}} \tag{4}$$

The comparison of intergranular strains $\left(\varepsilon^{I}_{hkl}\right)$ matches the stress and plastic strains (ε_{p}) relationship as shown in Eq. (5), which concerns the effects of the dislocation density (Dieter, 1986).

$$\sigma \propto \alpha G b \sqrt{M} \sqrt{\varepsilon_{\mathrm{p}}} \tag{5}$$

Here the true stress (σ) is proportional to the shear modulus (G), Burgers vector (b), the multiplication factor (M), and the plastic strain (ε_{p}). The trend and quantity of $\varepsilon^{\mathrm{I}}_{hkl}$ from these two experiments are similar as shown in Figs. 8a and b, which suggest that, under the current experimental parameter, for this alloy, the hardening mechanism is mainly dominated by *dislocation hardening* in the true stress region (370–600) MPa. The following conclusion can be made for *dislocation hardening*: After the elastic region (Stage I), the increase of the true stress followed by the increase of lattice strain, results in the plastic deformation accompanied by the increase of the dislocation density and decrease of the dislocation-wall spacing. The decrease of the dislocation-wall spacing indicates the formation of a self-organized cell wall structure, where more dislocations start to accumulate within dislocation walls. More specifically, during plastic deformation, the energy of the alloy is partially stored as dislocations, which are not randomly distributed but accumulate in dislocation boundaries. Moreover, the FWHM versus $2\pi/d$ relationship associating with the stress reflects that the dislocation hardening is the major strengthening mechanism within these stress levels.

The reason for the different quantities of both dislocation density and dislocation-wall spacings from two types of deformation at the similar stress levels is discussed below. In fatigue experiments, it seems that the dislocations may annihilate each other in the course of cycling. The mutual annihilation of dislocations can take place during cyclic-loading, which results in a smaller dislocation density but wider dislocation-wall spacing (Figs. 6 and 7). As a result, even at the similar stress levels, the different quantities of dislocation densities and dislocation-wall spacings could indicate two types of loading. Further research is continued now for distinguishing the difference in details.

Although the differences of the dislocation density and wall spacing from two types of deformations are recognized, the comparisons of the dislocation characteristics within a fatigue cycle during low-cycle-fatigue experiments are still plausible from the statistics point of view. The symmetrical stress–strain response under tension and compression in the 1st fatigue cycle (Fig. 3a) for the low-cycle-fatigue experiments is in agreement with earlier observations of Mughrabi (1983) and Ungar et al. (1993).

For the dislocation characteristics from the low-cycle-fatigue experiments, the evolution of the dislocation density and dislocation-wall spacing are shown in Figs. 9a and b, respectively. Seven measurements within one fatigue cycle are presented to address Guinier and Julien (1989) question of the atomic mechanisms during fatigue deformation. At the 1st cycle, the Measurements 1, 4, and 7 have the higher dislocation density than the other measurements, which are in proportion to their stress. And the Measurement 7 has a higher dislocation density than that of the Measurement 1, which shows the dislocation hardening even within the 1st cycle. However, at the 100th fatigue cycle, where the cyclic softening was about to occur, the dislocation density decreases from Measurements 1–7 within one fatigue cycle. A relative little decreasing of dislocation density of the 1500th cycle in Fig. 9a agrees with the very little cyclic softening, as shown in Fig. 3b. The comparisons of the dislocation density at the seven measurements for three different fatigue cycles are shown in Fig. 9a. Although the same engineering strains/stresses were controlled for the 1st, 100th, and 1500th fatigue cycles during the measurements, the observed dislocation density within the 1st cycle is several times less than that of the 100th and the 1500th cycles, which shows the accumulation of the dislocation density during the cyclic hardening. Fig. 9b shows the dislocation-wall spacing. The dash line and larger legend size in Fig. 9b are used for the 1st fatigue cycle, where the calculated values are greater than 1500 nm (similar to Figs. 6b and 7b). The evolutions of dislocation-wall spacing in Fig. 9b shows the reverse trends where the spacing decreased during cyclic deformation after the 100th and 1500th cycles. The similar inverse relationship between dislocation density and dislocation-wall spacing was reported by Hansen (2001 and 2005).

Low-cycle-fatigue experiments

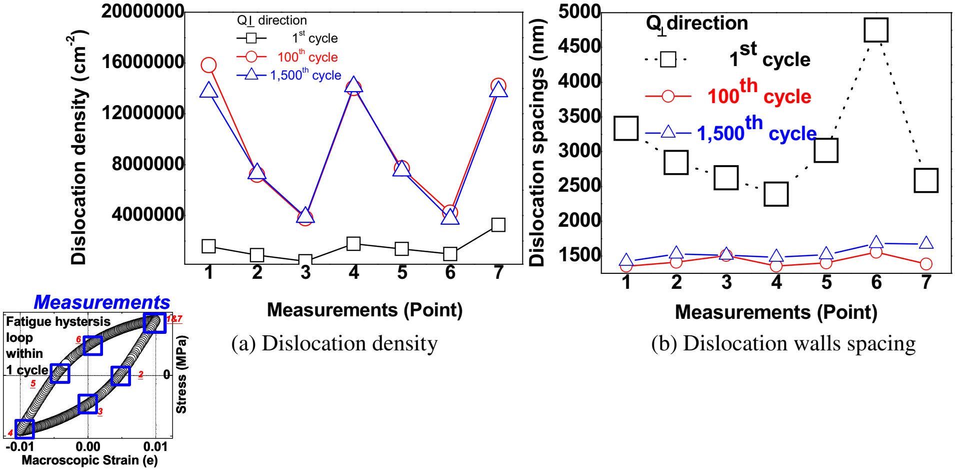

(a) Dislocation density

(b) Dislocation walls spacing

Fig. 9. (a) The dislocation density and (b) the dislocation-wall spacing evolutions within one fatigue cycle at 1st (black), 100th (red), and 1500th fatigue cycles in $Q_\perp$ direction. The conditions of seven measurements are shown in Fig. 3a as the insert.

Within one fatigue cycle, the dislocation-wall spacings of Measurements 1 (maximum tension strain), 4 (maximum compression strain), and 7 (maximum tension strain) were smaller than those of the other measurements, which were the inverse trends of the dislocation density as shown in Fig. 9a. The inverse relationship demonstrates that, while the dislocation density increased under the cyclic effects in the most strained/compressed status, the accumulation of the dislocation density and their rearrangement shortened the dislocation-wall spacing. The natural exception is the 1st measurement of the 1st fatigue cycle, where the monotonic-tension was just applied from 0 MPa to 1% engineering strain, but the cyclic deformation did not start yet. The variation between different measurements gradually decreases as the number of fatigue cycles increased. It seems that as the fatigue cycles increases within 1500 cycles, dislocation-wall spacing between dislocation multiplication and annihilation gradually reaches an equilibrium.

6. Summary

In-situ neutron-diffraction results were refined by GSAS. The pseudo-Voigt function was applied to distinguish between Gaussian and Lorentzian peak components. The density of dislocations and the average distance between dislocation walls were calculated accordingly to characterize the bulk response during the plastic deformation. Hence, the neutron-diffraction profiles were used to characterize the dislocation distributions. For this alloy, there was practically no accumulation of dislocations in the elastic region (Stage I). Within 370–600 MPa, the dislocation hardening was the major strengthening mechanism of the monotonic-tension and low-cycle-fatigue experiments. The dislocation density and the dislocation-wall spacing evolved accordingly within one fatigue cycle. Above 750 MPa, the dislocation-wall spacing evolved differently with dislocation density because the mechanical properties of dislocations within the walls are stiffer than those inside the cells, as described by Mughrabi's composite model. The same analysis method is applied to study the cyclically-deformed alloy. Different quantities of the dislocation density and dislocation-wall spacings demonstrate the ability of the diffraction profiles to distinguish different types of loading at similar applied loads. For low-cycle-fatigue experiments, the calculated dislocation density and dislocation-wall spacing are promising indicators for characterizing the cyclical hardening and early softening phenomena within 1500 fatigue cycles of the alloy.

Acknowledgements

This research is supported by the National Science Foundation (NSF), International Materials Institutes (IMI) Program (DMR-0231320). Dr. Carmen Huber is the Director of the IMI program. Research (R.B. and G.I.) sponsored by the Division of Materials Science and Engineering, Office of Basic Energy Science, US Department of Energy, under Contract DE-AC05-00OR22725 with UT-Battelle, LLC. The Lujan Neutron Scattering Center at LANSCE is funded by the Department of Energy's Office of Basic Energy Science. The Los Alamos National Laboratory is operated by the Los Alamos National Security LLC under the DOE Contract DE-AC52-06NA25396. Use of the Advanced Photon Source was supported by the US Department of Energy, Office of Science, Office of Basic Energy Science, under Contract No. DE-AC02-CH11357.

References

Balzar, D., Audebrand, N., Daymond, M.R., Fitch, A., Hewat, A., Langford, J.I., Le Bail, A., Louer, D., Masson, O., McCowan, C.N., Popa, N.C., Stephens, P.W., Toby, B.H., 2004. Size-strain line-broadening analysis of the ceria round-robin sample. J. Appl. Cryst. 37, 911–924.

Barabash, R.I., 2001. X-ray and neutron scattering by different dislocation ensembles. Mater. Sci. Eng. A, 49–54.

Barabash, R.I., Ice, G.E., Walker, F., 2003. Quantitative microdiffraction from deformed crystals with unpaired dislocations and dislocation walls. J. Appl. Phys. 93 (3), 1457–1464.

Benson, M.L., Liaw, P.K., Saleh, T.A., Choo, H., Brown, D.W., Daymond, M.R., Huang, E.-W., Wang, X.-L., Stoica, A.D., Buchanan, R.A., Klarstrom, D.L., 2006. Deformation-induced phase development in a cobalt-based superalloy during monotonic and cyclic deformation. Physica B, 523–525.

Bernier, J.V., Miller, M.P., 2006. A direct method for determination of the mean orientation-dependent elastic strains and stresses in polycrystalline materials from strain pole figures. J. Appl. Crystallogr. 39, 358–368.

Bourke, M.A.M., Dunand, D.C., Ustundag, E., 2002. SMARTS – a spectrometer for strain measurement in engineering materials. Appl. Phys. A 74, 1707–1709.

Brown, D.W., Bourke, M.A.M., Clausen, B., Holden, T.M., Tome, C.N., Varma, R., 2003. A neutron diffraction and modeling study of uniaxial deformation in polycrystalline beryllium. Metall. Mater. Trans. A 34, 1439–1449.

Daymond, M.R., Bourke, M.A.M., Von Dreele, R.B., Clausen, B., Lorentzen, T., 1997. Use Rietveld refinement for elastic macrostrain determination and for evaluation of plastic strain history from diffraction spectra. J. Appl. Phys. 82 (4), 1554–1562.

Dieter, G.E., 1986. Mechanical Metallurgy, third ed. McGraw-Hill, New York, pp. 103–324.

Guinier, A., Julien, R., 1989. The Solid State from Superconductors to Superalloys. Oxford Science Publications, New York, pp. 190–241.

Hansen, N., 2001. New discoveries in deformed metals. Metall. Mater. Trans. A 32, 2917–2935.

Hansen, N., 2005. Boundary strengthening over five length scales. Adv. Eng. Mater. A 32, 2917–2935.

Hirsch, P.B., Whelan, M.J., 1960. A kinematical theory of diffraction contrast of electron transmission microscope images of dislocations and other defects. Philos. Trans. R. Soc. Lond. Ser. A 252, 499–529.

Howie, A., Whelan, M.J., 1962. Diffraction contrast of electron microscope images of crystal lattice defects. III. Results and experimental confirmation of the dynamical theory of dislocation image contrast. Proc. R. Soc. Lond. Ser. A 267, 206–230.

Huang, E-W., Clausen, B., Wang, Y.D., Choo, H., Liaw, P.K., Benson, M.L., Pike, L.M., Klarstrom, D.L., 2007. A neutron-diffraction study of the low-cycle fatigue behavior of Hastelloy C-22HS™ alloy. Int. J. Fatigue 29, 1812–1819.

Ice, G.E., Barabash, R.I., 2007. White beam microdiffraction and dislocations gradients, in series. Dislocat. Solid 13 (79), 500–601.

Jakobsen, B., Lienert, U., Almer, J., Shastri, S.D., Sorensen, H.O., Gundlach, C., Pantleon, W., 2006. Formation and subdivision of deformation structures during plastic deformation. Science 312, 889–892.

Kuhlmann-Wilsdorf, D., 1962. A new theory of work hardening. Trans. Met. Soc. AIME 224, 1047–1062.

Kuhlmann-Wilsdorf, D., 1999. The theory of dislocation-based crystal plasticity. Philos. Mag. A 79 (4), 955–1008.

Levine, L.E., Larson, B.C., Yang, W., Kassner, M.E., Tischler, J.Z., Delos-Reyes, M.A., Fields, R.J., Liu, W., 2006. X-ray microdiffraction measurements of individual dislocation cell elastic strains in deformed single-crystal copper. Nat. Mater. 5, 619–622.

Liu, Q., Jensen, D.J., Hansen, N., 1998. Effect of grain orientation on deformation structure in cold-rolled polycrystalline aluminum. Acta Mater. 46, 5819–5838.

Lu, Y.L., Pike, L.M., Brooks, C.R., Liaw, P.K., Klarstrom, D.L., 2007. Strengthening domains in a Ni–21Cr–17Mo alloy. Scripta Mater. 56, 121–124.

Margulies, L., Winther, G., Poulsen, H.F., 2001. In situ measurement of grain rotation during deformation of polycrystals. Science 291, 2392–2394.

Miller, M.P., Bernier, J.V., Park, J.-S., Kazimirov, 2005. Experimental measurement of lattice strain pole figures using synchrotron X-rays. Rev. Sci. Instrum. 76, 113903.

Mughrabi, H., 1983. Dislocation wall and cell structures and long-range internal stresses in deformed metal crystals. Acta Metall. 31 (9), 1367–1379.

Rietveld, H.M., 1967. Line profiles of neutron powder-diffraction peaks for structure refinement. Acta Cryst. 22, 151.

Stephens, P.W., 1999. Phenomenological model of anisotropic peak broadening in powder diffraction. J. Appl. Cryst. 32, 281–289.

Sun, Y., Barabash, R.I., Choo, H., Liaw, P.K., Lu, Y., Brown, D.W., Ice, G.E., 2007. Multiscale plastic deformation near a fatigue crack from diffraction. Solid State Phenom. 129, 151–156.

Turkmen, H.S., Dawson, P.R., Miller, M.P., 2002. The evolution of crystalline stresses of a polycrystalline metal during cyclic loading. Int. J. Plasticity 18, 941–969.

Ungar, T., Biermann, H., Mughrabi, H., 1993. Dislocation distributions as seen by X-ray line profiles. Mater. Sci. Eng. A 164, 175–179.

Ungar, T., Dragomir, I., Revesz, A., Borbely, A., 1999. The contrast factors of dislocations in cubic crystals: the dislocation model of strain anisotropy in practice. J. Appl. Cryst. 32, 992–1002.

Valiev, R.Z., Islamgaliev, R.K., Alexandrov, I.V., 2000. Bulk nanostructured materials from severe plastic deformation. Prog. Mater. Sci. 45, 103–189.

Von Dreele, R.B., Jorgensen, J.D., Windsor, C.G., 1982. Rietveld refinement with spallation neutron powder diffraction data. J. Appl. Cryst. 15, 581–589.

Von Dreele, R.B., 2004. General structure analysis system. Los Alamos National Laboratory Report LAUR 86-748, pp. 160–165.

Wang, Y.-D., Tian, H., Stoica, A.D., Wang, X.-L., Liaw, P.K., Richardson, J.W., 2003. The development of grain-orientation-dependent residual stresses in a cyclically deformed alloy. Nature Mater. 2, 101–106.

Wenk, H.R., Grigull, S., 2003. Synchrotron texture analysis with area detectors. J. Appl. Cryst. 36, 1040–1049.